

A Tale of two Higgs: Search for pair
production of Higgs bosons in the $b\bar{b}b\bar{b}$
final state using proton–proton collisions at
 $\sqrt{s} = 13$ TeV with the ATLAS detector

A DISSERTATION PRESENTED
BY
BAOJIA TONG
TO
THE DEPARTMENT OF PHYSICS

IN PARTIAL FULFILLMENT OF THE REQUIREMENTS
FOR THE DEGREE OF
DOCTOR OF PHILOSOPHY
IN THE SUBJECT OF
PHYSICS

HARVARD UNIVERSITY
CAMBRIDGE, MASSACHUSETTS
MAY 2018

©2017-2018 – BAOJIA TONG
ALL RIGHTS RESERVED.

A Tale of two Higgs: Search for pair production of Higgs bosons in the $b\bar{b}b\bar{b}$ final state using proton–proton collisions at $\sqrt{s} = 13$ TeV with the ATLAS detector

ABSTRACT

This thesis presents a search for Higgs boson pair production, with the $b\bar{b}b\bar{b}$ final state. This search uses the full 2015 and 2016 data collected by the ATLAS Collaboration at $\sqrt{s} = 13$ TeV, corresponding to $3.2 \pm 0.2 \text{ fb}^{-1}$ of 2015 and $32.9 \pm 1.1 \text{ fb}^{-1}$ of 2016 pp collision data. Improvements with respect to the previous analysis come from the increased dataset, detailed background estimation and additional signal regions. Search sensitivity is specially enhanced for the resonance signals between 2500 GeV and 3000 GeV. The data is found to be compatible with the Standard Model predictions, and no signs of new physics have been observed. The results are interpreted in the context of the bulk Randall-Sundrum warped extra dimension model with a Kaluza-Klein graviton $k/\bar{M}_{\text{Pl}} = 1.0$ or 2.0 decaying to hh , and the Type 2 two-Higgs doublet model (2HDM) where the neutral heavy CP-even H scalar decays to hh .

Contents

o INTRODUCTION	I
1 THEORY AND MOTIVATION	5
1.1 The Standard Model and the Higgs Boson	5
1.2 Standard Model di-Higgs production	7
1.3 Beyond the Standard Model physics di-Higgs production	9
1.4 Di-Higgs decay and LHC previous search results	13
2 LHC AND ATLAS	16
2.1 The Large Hadron Collider	16
2.2 A Toroidal LHC ApparatuS	19
3 RECONSTRUCTION AND OBJECTS	25
3.1 Jets	26
3.2 Boost	30
3.3 Flavor Tagging	31
3.4 Leptons	33
4 DATA AND SIMULATION	35
5 CONCLUSION	37
REFERENCES	39

Listing of figures

<p>1.1 Fermions and bosons of the Standard Model and their properties¹, where all the values are measured experimentally.</p> <p>1.2 Leading order Feynman diagrams contributing to di-Higgs production via gluon-gluon fusion, through the Higgs-fermion Yukawa interactions 1.2a and the Higgs boson self-coupling 1.2b. Only Figure 1.2b probes λ_{hhh}.</p> <p>1.3 Total cross sections (y-axis) at the NLO in QCD for the six largest di-Higgs production channels at p-p colliders at different energy (x-axis). The thickness of the lines corresponds to the scale and PDF uncertainties added linearly. H refers to the SM Higgs.</p> <p>1.4 BSM Higgs boson pair production: non-resonant production proceeds through changes in the SM Higgs couplings in 1.4a and 1.4b, resonant production proceeds through 1.4c an intermediate resonance, X. H and b both refers to the SM Higgs.</p> <p>1.5 Total cross sections (y-axis) at the LO and NLO in QCD for di-Higgs production channels, at the $\sqrt{s} = 14$ TeV LHC as a function of the self-interaction coupling λ (x-axis) . The dashed (solid) lines and light- (dark-) color bands correspond to the LO (NLO) results and to the scale and PDF uncertainties added linearly. The SM values of the cross sections are obtained at $\frac{\lambda}{\lambda_{SM}} = 1$. H refers to the SM Higgs.</p> <p>1.6 Parton luminosity ratios as a function of resonance mass M_X for $13/8$ TeV². For a 2 TeV X, the luminosity ratio is almost 10.</p> <p>1.7 Summary of di-Higgs final states and their ratios. Top left, $b\bar{b}b\bar{b}$, has the largest branching ratio.</p> <p>1.8 The observed and expected 95% CL upper limits of $\sigma(gg \rightarrow H) \times BR(H \rightarrow bb)$ at $\sqrt{s} = 8$ TeV as functions of the heavy Higgs boson mass m_H, combining resonant searches in Higgs boson pair to $b\bar{b}\tau^+\tau^-$, $W^+W^-\gamma\gamma$, $b\bar{b}\gamma\gamma$, and $b\bar{b}b\bar{b}$ final states. The expected limits from individual searches are also shown. The green and yellow bands represent $\pm 1\sigma$ and $\pm 2\sigma$ uncertainty ranges of the expected combined limits. The improvement above $m_H = 500$ GeV reflects the sensitivity of the $b\bar{b}b\bar{b}$ analysis. The results beyond 1 TeV are only from the $b\bar{b}b\bar{b}$ final state alone.</p>	<p>6</p> <p>7</p> <p>8</p> <p>9</p> <p>10</p> <p>12</p> <p>13</p> <p>14</p>
--	---

2.1	A schematic view of the LHC ring ³ . LINAC ₂ , Booster, PS, SPS, and LHC accelerate the protons in order. Four main experiments are located at interaction points along the ring. ATLAS and CMS are general purpose experiments, while ALICE focuses on heavy ion collisions and LHC _b is dedicated to B physics.	17
2.2	The luminosity-weighted distribution of the mean number of interactions per crossing for the 2015 and 2016 pp collision data at 13 TeV centre-of-mass energy. ⁴	19
2.3	A detailed computer-generated image of the ATLAS detector and its systems.	19
2.4	Gemoetry of IBL, PIXEL and SCT detectors in Run2.	22
2.5	The overall layout of the ATLAS MuonSpectrometer.	23
2.6	Cumulative luminosity versus time delivered to (green) and recorded by ATLAS (yellow) during stable beams for pp collisions at 13 TeV centre-of-mass energy.	24
3.1	Illustration of particle interactions in ATLAS.	26
3.2	Uncalibrated (dashed line) and calibrated (solid line) reconstructed jet mass distribution 3.2a, and the jet mass resolution vs jet p_T 3.2b for calorimeter-based jet mass, mcalo (red), track-assisted jet mass mTA (black) and the invariant mass of four-vector sum of tracks associated to the large-radius calorimeter jet mtrack (blue) for W/Z-jets ⁵	28
3.3	Secondary vertex reconstruction rate and Mv2c10 output for b-jets (solid blue), c-jets (dashed green) and light-jets (dotted red) evaluated with $t\bar{t}$ events.	32

Listing of tables

2.1 LHC nominal and operational parameters	20
--	----

VERITAS SHALL MAKE YOU FREE.

Acknowledgments

THANKS TO EVERYONE WORKING AT CERN. CERN is a unique and special place. I love how the streets are named by physicists. Without the support from the IT department, I could not log into lxplus, check the twikis and finish my work. CERN user's office also made traveling to Europe a much nicer and easier experience for me.

THANKS TO EVERYONE WORKING ON THE LARGE HADRON COLLIDER. Without a fully functional accelerator, there would have been no data for me to study. The LHC performed outstandingly since 2015, and all the valuable data in this thesis is produced from it.

THANKS TO EVERYONE THE ATLAS COLLABORATION, who has supported this remarkable program and has contributed to every bit of the result in my thesis. I am standing on the ATLAS(member)'s shoulders—eight floors high and don't shrug. Without the excellent work on detector design, commissioning, operational works, reconstruction, data processing, performance studies and recommendations, software support, computing support, and analysis discussions and guidance, I could not have completed this thesis. I sincerely thank all ATLAS members for their work.

*It was the best of times, it was the worst of times, it was
the age of wisdom, it was the age of foolishness, it was
the epoch of belief, it was the epoch of incredulity, it
was the season of Light, it was the season of Darkness,
it was the spring of hope, it was the winter of despair,
we had everything before us, we had nothing before us,
we were all going direct to Heaven, we were all going
direct the other way—in short, the period was so far like
the present period, that some of its noisiest authorities
insisted on its being received, for good or for evil, in the
superlative degree of comparison only.*

Charles Dickens

0

Introduction

In 2012, the Higgs boson was discovered by the ATLAS and CMS experiment at the LHC. The particle physics community faces a period just like at the beginning of *A Tale of Two Cities*.

After Run 1 of the LHC, with the existence of the Higgs now firmly established, the focus shifted to searches for physics beyond the Standard Model.

In particular, searches for high mass resonances benefit from the LHC’s increase to $\sqrt{s} = 13$ TeV in Run 2. The cross section for a generic gluon-initiated resonance with a mass of 2 TeV increases tenfold in Run 2, making searches for high mass resonances a high priority. The newly discovered Higgs can be used as a tool in these searches. After the discovery, the Higgs boson provides a large swath of unmeasured phase space where new physics could be discovered. Higgs pair production in the Standard Model has a low cross section that requires large datasets (on the order of the

LHC's lifetime) for full measurement. However, new physics can modify this cross section, especially through new resonances which decay to two Higgs bosons. Such high mass resonances also produce difficult to recognize final state topologies due to the merging of decay products from high momentum Higgs bosons. A search for Higgs pair production in the $HH \rightarrow b\bar{b}b\bar{b}$ final state was performed with 3.2fb^{-1} collected with ATLAS at $\sqrt{s} = 13$ TeV in 2015. The results are presented in this dissertation with a focus on a dedicated signal region for boosted final states. This signal region uses new techniques for recognizing jet substructure and b -tagging to improve signal acceptance of high mass resonances.

The discovery of the Standard Model (SM) Higgs boson (h)² at the Large Hadron Collider (LHC) motivates searches for new physics using the Higgs boson as a probe. In particular, many models predict cross sections for Higgs boson pair production that are significantly greater than the SM prediction. Resonant Higgs boson pair production is predicted by models such as the bulk Randall–Sundrum model^{6,7}, which features spin-2 Kaluza–Klein gravitons, G_{KK}^* , that subsequently decay to a pair of Higgs bosons. Extensions of the Higgs sector, such as two-Higgs-doublet models^{8,9}, propose the existence of a heavy spin-0 scalar that can decay into h pairs. Enhanced non-resonant Higgs boson pair production is predicted by other models, for example those featuring light coloured scalars¹⁰ or direct $t\bar{t}hh$ vertices^{11,12}.

Previous searches for Higgs boson pair production have all yielded null results. In the $b\bar{b}b\bar{b}$ channel, ATLAS searched for both non-resonant and resonant production in the mass range of 400–3000 GeV using 3.2 fb^{-1} of 13 TeV data¹³ collected during 2015. CMS searched for the production of resonances with masses of 750–3000 GeV² using 13 TeV data and with masses 270–1100 GeV with 8 TeV data². Using 8 TeV data, ATLAS has examined the $b\bar{b}b\bar{b}$ ¹⁴, $b\bar{b}\gamma\gamma$ ¹⁵, $b\bar{b}\tau^+\tau^-$ and $W^+W^-\gamma\gamma$ channels, all of which were combined in Ref.². CMS has performed searches using 13 TeV data for the $b\bar{b}\tau^+\tau^-$ ² and $b\bar{b}\ell\nu\ell\nu$ ² final states, and used 8 TeV data to search for $b\bar{b}\gamma\gamma$ ² in addition to a search in multilepton and multilepton+photons final states².

The analyses presented in this paper exploit the dominant $b \rightarrow b\bar{b}$ decay mode to search for Higgs boson pair production in both resonant and non-resonant production. Two analyses are presented, which are complementary in their acceptance, each employing a unique technique to reconstruct the Higgs boson. The “resolved” analysis is used for hh systems in which the Higgs bosons have Lorentz boosts low enough that four b -jets can be reconstructed. The “boosted” analysis is used for those hh systems in which the Higgs bosons have higher Lorentz boosts, which prevents the Higgs boson decay products from being resolved in the detector as separate b -jets. Instead, each Higgs boson candidate consists of a single large-radius jet, and b -decays are identified using smaller-radius jets built from charged-particle tracks.

Both analyses were re-optimized with respect to the former ATLAS publication¹³; an improved algorithm to pair b -jets to Higgs boson candidates is used in the resolved analysis, and in the boosted analysis an additional signal-enriched sample is utilized. The dataset comprises the 2015 and 2016 data, corresponding to 27.5 fb^{-1} for the resolved analysis and 36.1 fb^{-1} for the boosted analysis, with the difference due to the trigger selections used. The results are obtained using the resolved analysis for a resonance mass between 260 and 1400 GeV, and the boosted analysis between 800 GeV and 3000 GeV. The main background is multijet production, which is estimated from data; the sub-leading background is $t\bar{t}$, which is estimated using both data and simulations. The two analyses employ orthogonal selections, and a statistical combination is performed in the mass range where they overlap. The final discriminants are the four-jet and dijet mass distributions in the resolved and boosted analyses, respectively. Searches are performed for the following benchmark signals: a spin-2 graviton decaying into Higgs bosons, a scalar resonance decaying into a Higgs boson pair, and SM non-resonant Higgs boson pair production.

This dissertation begins by discussing the status of di-Higgs. Chapter 1 gives an overview of double Higgs production in the Standard Model and beyond. Chapter 2 and 3 present details regarding

the Large Hadron Collider and the ATLAS experiment. Chapter 4 provides an overview of object reconstruction in ATLAS, with a focus on Muon Segment Seeding. A brief interlude in Chapter 5 on the ATLAS Muon Data Quality, as this has been a focus of my graduate work.

The rest of the dissertation presents a search for Higgs pair production in the $HH \rightarrow b\bar{b}b\bar{b}$ channel. Chapter 6 presents an overview of physics object selection, where the Higgs pairs are the result of the decay of a heavy resonance. Chapter 7 discusses the background estimation techninics in detail, followed by Chapter 8, Systematics. Chapter 9 presents the results, and Chapter 10 shows the limits between the boosted regime and the resolved regime, which is sensitive to lower mass resonances and non-resonant Higgs pair production. Finally, the work is summarized a conclusion and brief outlook of future Higgs physics with ATLAS.

Knowledge knows no bounds.

Creator

1

Theory and Motivation

1.1 THE STANDARD MODEL AND THE HIGGS BOSON

The Standard Model(SM)^{1,16,17,18} is a quantum field theory describing the interactions of fundamental particles. The particles are shown in Figure 1.1. So far, the SM predictions agree extremely well with experimental observations.

In the SM, the Higgs mechanism introduces a complex scalar Higgs field, ϕ , with nonzero vacuum expectation values. The scalar Higgs potential is $V(\phi) = -v^2\lambda_v\phi^\dagger\phi + \lambda_v(\phi^\dagger\phi)^2$. Through spontaneous symmetry breaking, W^\pm and Z bosons acquire their masses. This process also predicts an extra scalar, the Higgs boson. The SM Lagrangian containing Higgs couplings, $\mathcal{L}_{\text{Higgs}}$, is shown

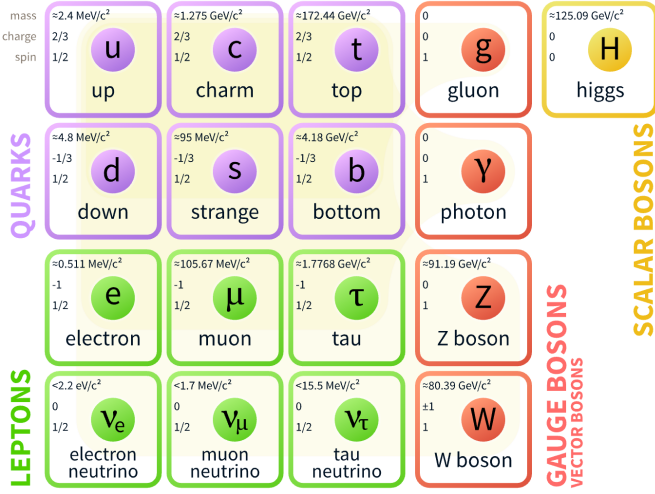


Figure 1.1: Fermions and bosons of the Standard Model and their properties¹, where all the values are measured experimentally.

in Eq 1.1.

$$\mathcal{L}_{\text{Higgs}} = -\lambda_{h\bar{f}f} h\bar{f}f + \delta_V V_\mu V^\mu (\lambda_{hvv} b + \lambda_{hhvv} b^2) + \lambda_{hh} b^2 + \lambda_{hhh} b^3 + \lambda_{hhhh} b^4 \quad (1.1)$$

where

- $v \sim 246 \text{ GeV}$, is the non-zero expectation value of the Higgs field;
- $m_h = \sqrt{2\lambda_v} v \sim 125 \text{ GeV}$, is the Higgs mass; this is discovered in 2012^{19,20};
- λ_v , coefficient for the quartic potential term, is constrained from Higgs mass, to be ~ -0.13 ;
- $V = W^\pm$ or Z , $\delta_W = 1$, $\delta_Z = \frac{1}{2}$;
- $\lambda_{h\bar{f}f} = \frac{m_f}{v}$, is the Higgs to fermion coupling; m_f is the mass of the fermion;
- $\lambda_{hvv} = \frac{2m_v^2}{v}$, is the Higgs to boson coupling; m_v is the mass of the boson;
- $\lambda_{hhvv} = \frac{m_v^2}{v^2}$, is the Higgs-Higgs to boson-boson coupling;
- $\lambda_{hh} = \frac{m_h^2}{2}$, is the Higgs mass term;

- $\lambda_{hhh} = \frac{m_h^2}{2\nu} = \lambda_{\nu\nu}$, or λ_{hhh} , is the Higgs self-coupling;
- $\lambda_{hhh} = \frac{m_h^2}{8\nu^2}$, is the Higgs quartic-coupling.

What's particularly interesting and has not been measured experimentally in Eq 1.1 is λ_{hhh} . SM predicts $\lambda_{hhh} = \frac{m_h^2}{2\nu}$, which is referred as λ_{SM} in this thesis. This term directly probes the Higgs potential. Also, $\lambda_{hhh} h^3$ term shows one way for double Higgs production within the SM. Double Higgs production is also known as di-Higgs or Higgs pair production.

1.2 STANDARD MODEL DI-HIGGS PRODUCTION

There are two main production diagrams of di-Higgs at the LHC, shown in Figure 1.2. In the gluon-gluon fusion process, di-Higgs are produced through a box or a triangle loop. Only the triangle loop 1.2b probes the λ_{hhh} . In the triangle diagram, the middle Higgs boson acts as a propagator (off-shell), and the two Higgs boson in the final state are on-shell. An on-shell middle Higgs, with two off-shell Higgs bosons in the final state, is strongly disfavored¹. The box and triangle diagrams interfere destructively, which makes the overall production rate smaller than what would be expected in the absence of a λ_{hhh} term.

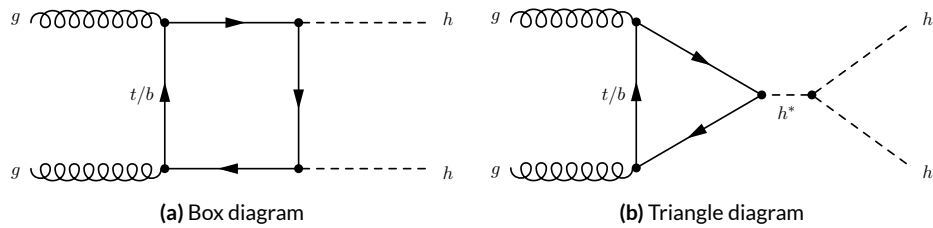


Figure 1.2: Leading order Feynman diagrams contributing to di-Higgs production via gluon-gluon fusion, through the Higgs-fermion Yukawa interactions 1.2a and the Higgs boson self-coupling 1.2b. Only Figure 1.2b probes λ_{hhh} .

Many other different production modes of di-Higgs exist, but gluon-gluon fusion is the dominant one. Figure 1.3²¹ compares the cross sections of gluon-gluon fusion, Vector Boson Fusion (VBF), and top-pair, W^\pm , Z and single-top associated di-Higgs production.

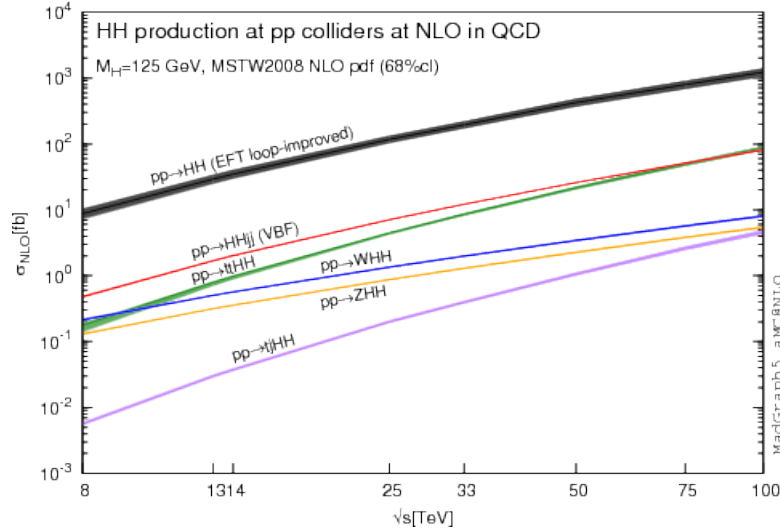


Figure 1.3: Total cross sections (y-axis) at the NLO in QCD for the six largest di-Higgs production channels at p-p colliders at different energy (x-axis). The thickness of the lines corresponds to the scale and PDF uncertainties added linearly. H refers to the SM Higgs.

For p-p collisions at $\sqrt{s} = 13$ TeV, the total cross section for SM gluon fusion di-Higgs production²², at the Next to Next Leading Order (NNLO) with top quark mass effects, is $33.49^{+4.3\%}_{-6.0\%} \pm 2.1\% \pm 2.3\%$ fb. The cross section for the next dominant production, VBF, is $1.62^{+2.3\%}_{-2.7\%} \pm 2.3\%$ fb. The estimated cross section for triple-Higgs production is $0.06332^{+16.1\%}_{-14.1\%} \pm 3.4\%$ fb, which is negligible with current dataset. The uncertainties are Scale uncertainty, PDF uncertainty and α_s uncertainty. This means inside 2015 and 2016 $\sqrt{s} = 13$ TeV ATLAS 36 fb⁻¹ data, there are only around one thousand SM di-Higgs events.

1.3 BEYOND THE STANDARD MODEL PHYSICS DI-HIGGS PRODUCTION

The SM works extremely well, yet the Higgs boson mass at 125 GeV requires extreme fine-tuning for radiative corrections. The presence of new physics at the TeV scale would help solve the naturalness problem.

BSM physics could significantly enhance the production of di-Higgs at the LHC. This is separated into two categories: non-resonant and resonant productions. The non-resonant production generally refers to modifications of the Higgs couplings, either the Higgs self-coupling or the Higgs-top couplings. Resonant production refers to a particle with invariant mass greater than twice the Higgs mass decays directly into two Higgs bosons. The difference also comes from the distribution of the di-Higgs invariant mass at the truth level. In the non-resonant case, the distribution has no clear peak, whereas in the resonant case, the invariant mass distribution usually forms a peak with model dependent width.

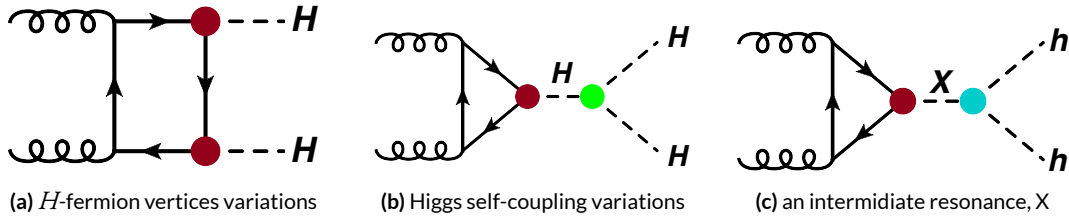


Figure 1.4: BSM Higgs boson pair production: non-resonant production proceeds through changes in the SM Higgs couplings in 1.4a and 1.4b, resonant production proceeds through 1.4c an intermediate resonance, X . H and h both refers to the SM Higgs.

1.3.1 BSM NON-RESONANT DI-HIGGS

Enhanced non-resonant Higgs boson pair production is predicted by many models. Models featuring direct $t\bar{t}hh$ vertices^{11,12} or new light colored scalars¹⁰ could change vertices shown as the red

dots in Figure 1.4. A direct modification of Higgs self-coupling term in Eq 1.1 to λbhh , where λ is different from λ_{SM} , is also possible. This is shown as the green dot in Figure 1.4b.

The non-resonant di-Higgs enhancement is usually described by $\frac{\lambda}{\lambda_{\text{SM}}}$, which is the cross section ratio between λ and λ_{SM} . From the SM electroweak measurements, the self coupling term could be constrained to $-14 \leq \frac{\lambda}{\lambda_{\text{SM}}} \leq 17.4$ ²³. Variations of λ have a non-trivial effect on di-Higgs production cross section, shown in Figure 1.5²¹. In the regime of relatively high trilinear coupling, the observation will be an excess of di-Higgs events with respect to the expected background. A simple limit can be set in this case.

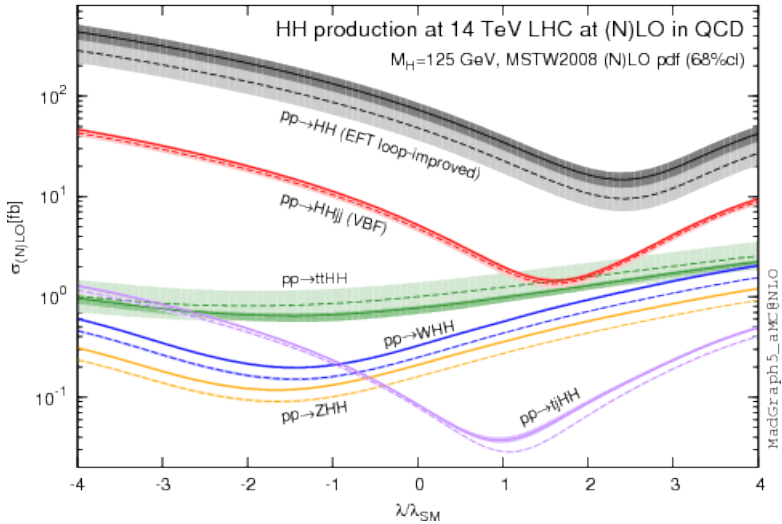


Figure 1.5: Total cross sections (y-axis) at the LO and NLO in QCD for di-Higgs production channels, at the $\sqrt{s} = 14$ TeV LHC as a function of the self-interaction coupling λ (x-axis). The dashed (solid) lines and light- (dark-) color bands correspond to the LO (NLO) results and to the scale and PDF uncertainties added linearly. The SM values of the cross sections are obtained at $\frac{\lambda}{\lambda_{\text{SM}}} = 1$. H refers to the SM Higgs.

1.3.2 BSM RESONANT DI-HIGGS

Resonant Higgs boson pair production is also predicted by many models. Extensions of the Higgs sector, such as two-Higgs-doublet models(2HDM)^{8,9}, propose the existence of a heavy spin-0 scalar

H that can decay into di-Higgs. The bulk Randall-Sundrum model^{6,7}, which features spin-2 Kaluza-Klein gravitons, G_{KK}^* , could also subsequently decay to pairs of Higgs bosons. These proposed heavy particles, heavy CP-even scalar H and G_{KK}^* , are represented as X in Figure 1.4c.

The 2HDM is a simple extension of the SM which can exhibit large resonance effects²². The 2HDM has 5 physical Higgs bosons: h (light scalar Higgs), H (heavy scalar Higgs), A (heavy pseudoscalar Higgs), and H^\pm (two charged Higgs). The 2HDM can introduce tree level flavor changing neutral currents. To avoid this, models impose discrete symmetries in which the charged fermions only couple to one of the Higgs doublets. One version is type II 2HDM, in which all positively charged quarks couple to one doublet and the negatively charged quarks and leptons couple to the other. The type II model is the Minimal Supersymmetric Standard Model(MSSM)'s Higgs sector.

Resonant di-Higgs production in 2HDM models can proceed through decays of the heavy CP-even Higgs $H \rightarrow hh$. The branching ratio for $H \rightarrow hh$ depends on the model type as well as the values of $\tan \beta$ and $\cos(\beta - \alpha)$. $\tan \beta = \frac{v_{\text{doublet}}}{v_{\text{SM}}}$ is the ratio of the vacuum expectation values of the two Higgs doublets. α is the mixing angle between the heavy H and light h fields. The limit where $\cos(\beta - \alpha) = 0$ is called the alignment limit, and in this limit the light Higgs h has the same couplings as a SM Higgs. Near the alignment limit there is some unprobed phase space depending on the exact models and values of $\tan \beta$ being considered, and they are particularly interesting to be searched for at the LHC.

The Randall-Sundrum model proposes a five-dimensional warped spacetime that contains two manifolds: one where the force of gravity is very strong and a second manifold at the TeV scale corresponding to the known SM sector. The experimental consequence of this theory is a series of widely mass-spaced Kaluza-Klein graviton resonances, G_{KK}^* . In theories where the fermions are localized to the SM brane, production of gravitons from fermion pairs is suppressed and the primary

mode of production of G_{KK}^* is gluon fusion. These gravitons have a substantial branching fraction to di-Higgs, ranging from 6.43% for gravitons with a mass of 500 GeV to 7.66% at 3 TeV. Randall-Sundrum models have two free parameters - the mass of the graviton and $c = k/\bar{M}_{\text{Pl}}$, where \bar{M}_{Pl} is the reduced Planck mass and k is the curvature parameter. The width of the graviton increases with both mass and c .

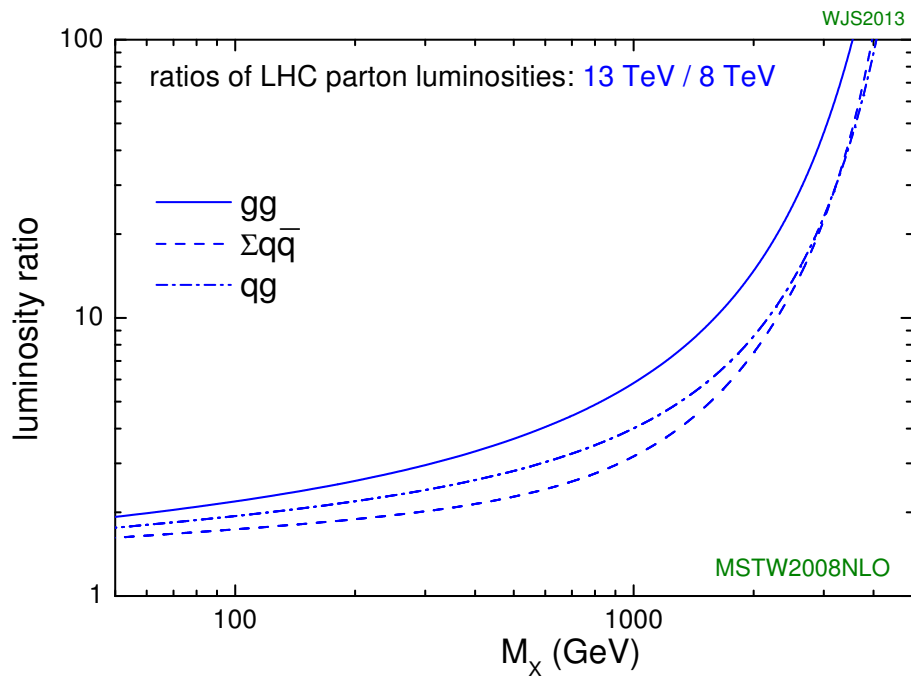


Figure 1.6: Parton luminosity ratios as a function of resonance mass M_X for 13/8 TeV². For a 2 TeV X , the luminosity ratio is almost 10.

In model dependent searches, based on fixed assumptions of the resonance particles' branching ratio, other search channels like resonance VV or $t\bar{t}$ are more sensitive compared to di-Higgs²⁴. In order to constrain more BSM physics phase space, di-Higgs search results need to be interpreted in different baseline models, covering both narrow and wide resonances.

Generally, it is easy theoretically for new heavy resonance particles to interact with the SM through the Higgs as a portal, resulting in resonance di-Higgs production. With the increased center of mass collision energy from 8 TeV to 13 TeV, the production cross section through gluon-gluon fusion for heavy particles above TeV grows in LHC Run 2, as shown in Figure 1.6. Therefore, it is particularly important to focus on resonant searches above TeV region.

1.4 DI-HIGGS DECAY AND LHC PREVIOUS SEARCH RESULTS

Di-Higgs decay is a combination of single Higgs decays. The coupling terms to fermions and bosons are shown in Eq 1.1. The branching ratio of the di-Higgs final state is shown in Figure 1.7.

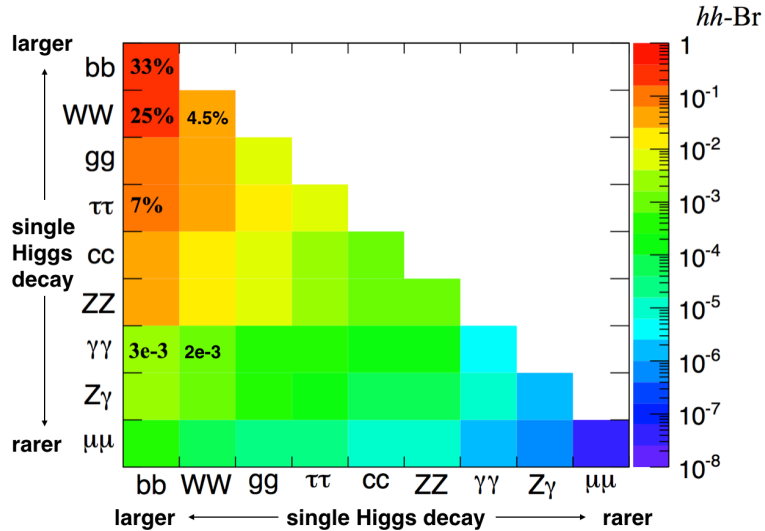


Figure 1.7: Summary of di-Higgs final states and their ratios. Top left, $b\bar{b}b\bar{b}$, has the largest branching ratio.

Previous searches for Higgs boson pair production have all yielded null results. Using 8 TeV data, ATLAS has examined the $b\bar{b}b\bar{b}$ ¹⁴, $b\bar{b}\gamma\gamma$ ¹⁵, $b\bar{b}\tau^+\tau^-$ and $W^+W^-\gamma\gamma$ channels, all of which were combined²⁵. The resonant search combination result is shown in Figure 1.8. The best non-resonant $\sigma(pp \rightarrow hh)$ cross section limit in Run 1 is the ATLAS combination, at 0.69 pb. This corresponds to

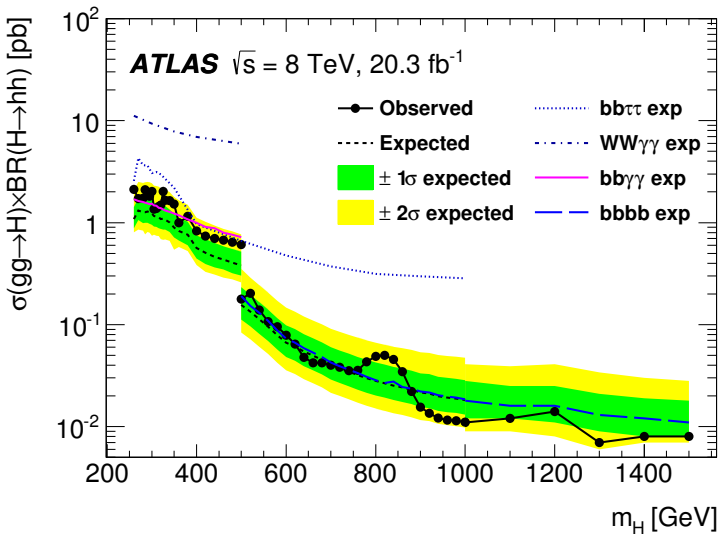


Figure 1.8: The observed and expected 95% CL upper limits of $\sigma(gg \rightarrow H) \times BR(H \rightarrow bb)$ at $\sqrt{s} = 8$ TeV as functions of the heavy Higgs boson mass m_H , combining resonant searches in Higgs boson pair to $b\bar{b}\tau^+\tau^-$, $W^+W^-\gamma\gamma$, $b\bar{b}\gamma\gamma$, and $b\bar{b}b\bar{b}$ final states. The expected limits from individual searches are also shown. The green and yellow bands represent $\pm 1\sigma$ and $\pm 2\sigma$ uncertainty ranges of the expected combined limits. The improvement above $m_H = 500$ GeV reflects the sensitivity of the $b\bar{b}b\bar{b}$ analysis. The results beyond 1 TeV are only from the $b\bar{b}b\bar{b}$ final state alone.

$\frac{\lambda}{\lambda_{SM}} < 70$. Different di-Higgs search challenges and perspectives are summarized below:

- $b\bar{b}b\bar{b}$: Trigger limits the low mass resonance searches, but for high mass resonances above 500 GeV, the branching ratio of this channel provides a decisive advantage. Great for non-resonant searches.
- $b\bar{b}W^+W^-$: Despite the second largest branching ratio, large background from $t\bar{t}$ limits this search sensitivity.
- $b\bar{b}\gamma\gamma$: Benefit from a good double photon trigger efficiency, a good photon reconstruction efficiency and a low SM background. Most sensitive at low mass $m_X \leq 350$ GeV. At higher masses, the smaller branching ratio and the merging of photons hurt the search sensitivity. Great for non-resonant searches.
- $b\bar{b}\tau^+\tau^-$: An intermediate choice between $b\bar{b}b\bar{b}$ and $b\bar{b}\gamma\gamma$ for resonance searches. Yet this channel contributes to the non-resonant result significantly.
- $W^+W^-\gamma\gamma$: Suffers from much lower branching ratio and lower reconstruction efficiency of the W^+W^- compared to $b\bar{b}$.

- $W^+W^-\tau\tau, W^+W^-W^+W^-, b\bar{b}ZZ$: There are no search results on these channels yet. But because of the relatively large branching ratio, it is likely that they would be explored in the future.

In summary, di-Higgs has a small production rate in the SM, but could be significantly enhanced in BSM scenarios. In particular, a heavy resonance spin-0 or spin 2 particle could decay into Higgs boson pair directly. The search sensitivity for massive resonances increases as the center of mass energy of the collision increases. For resonance signals above 1 TeV decaying into di-Higgs, $b\bar{b}b\bar{b}$ channel has the best discovery potential in Run 2. Therefore, searching for TeV scale resonance production of di-Higgs $\rightarrow b\bar{b}b\bar{b}$ is the goal of thesis.

Pain teaches lessons no scholar can.

2

LHC and ATLAS

The Large Hadron Collider (LHC) is a proton-proton collider at the European Organization for Nuclear Research (CERN) laboratory in Geneva, Switzerland²⁶. ATLAS (A Toroidal LHC ApparatuS), CMS (the Compact Muon Solenoid), ALICE (A Large Ion Collider Experiment), and LHCb^{27,28,29,30} are the four main experiments. They are located at the Interaction points(IPs) of the accelerator. Figure 2.1 shows a schematic of the LHC ring and its experiments.

2.1 THE LARGE HADRON COLLIDER

Protons accelerated in the LHC are from a red bottle of hydrogen gas. The whole acceleration takes around 25 minutes:

- An electric field strips the electrons from the hydrogen to create protons;

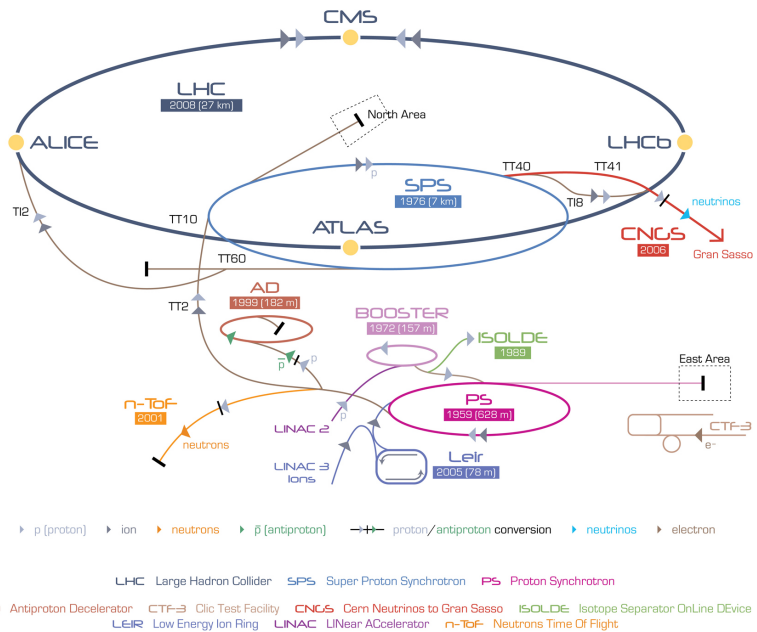


Figure 2.1: A schematic view of the LHC ring³. LINAC2, Booster, PS, SPS, and LHC accelerate the protons in order. Four main experiments are located at interaction points along the ring. ATLAS and CMS are general purpose experiments, while ALICE focuses on heavy ion collisions and LHC b is dedicated to B physics.

- A linear particle accelerator, Linac 2, accelerates the protons to 50 MeV;
- The Proton Synchrotron Booster (PSB) accelerates the protons to 1.4 GeV;
- The Proton Synchrotron (PS) accelerates the protons to 25 GeV;
- The Super Proton Synchrotron (SPS) accelerates the protons to 450 GeV; it sends the protons in bunch trains;
- The 16.7 kilometers LHC accelerates the protons in a series of Radio Frequency cavities to the final TeV energies. The LHC uses 1232 Niobium Titanium magnetic dipole for steering the protons. They are cooled by superfluid helium to 1.9 Kelvin, and can generate 8.33 Tesla magnetic field.

In proton-proton collisions, the rate of a certain physics process $R_{\text{phy}} = L\sigma$, where $L (m^{-2}s^{-1})$ is the instantaneous luminosity, and $\sigma(m^2)$ the cross section of physics process (like di-Higgs' $\sigma_{1.2}$).

For a Gaussian beam profile, the instantaneous luminosity is defined in Eq2.1 ³:

$$L = \frac{n_b N_b^2 f_{\text{rev}} \gamma_r}{4\pi \epsilon_n \beta^*} F \quad (2.1)$$

In the above Eq2.1:

- n_b is the number of bunches per beam; n_b cannot be too large due to potential beam loss damages on the accelerator and detector;
- N_b is the number of protons per bunch;
- f_{rev} is the proton revolution frequency;
- γ_r is the relativistic Lorentz factor for the protons;
- ϵ_n is the average beam spread length in the transverse plane;
- β^* is the beam spread in the longitudinal direction; affected by focusing magnets;
- F is a reduction factor for the angle beams are colliding; smaller crossing angles could cause larger spread in the longitudinal direction.

The instantaneous luminosity can also be written as the ratio of the rate of inelastic collisions to the inelastic cross section σ_{inel} ³:

$$L = \frac{R_{\text{inel}}}{\sigma_{\text{inel}}} = \frac{\mu n_b f_{\text{rev}}}{\sigma_{\text{inel}}} \quad (2.2)$$

where, μ is the number of interactions per bunch crossing. At each bunch crossing, multiple proton-proton collide, and the collisions without the highest center of mass energy are called “pileup” interactions. The target peak instantaneous luminosity for both the ATLAS and CMS experiments is $L = 10^{34} \text{ cm}^{-2}\text{s}^{-1}$ ²⁶, which is already exceeded in 2016. This is partly due to the rising number of “pileup” interactions, shown in Figure 2.2. The main parameters of the LHC beam and performance are shown in Table 2.1.

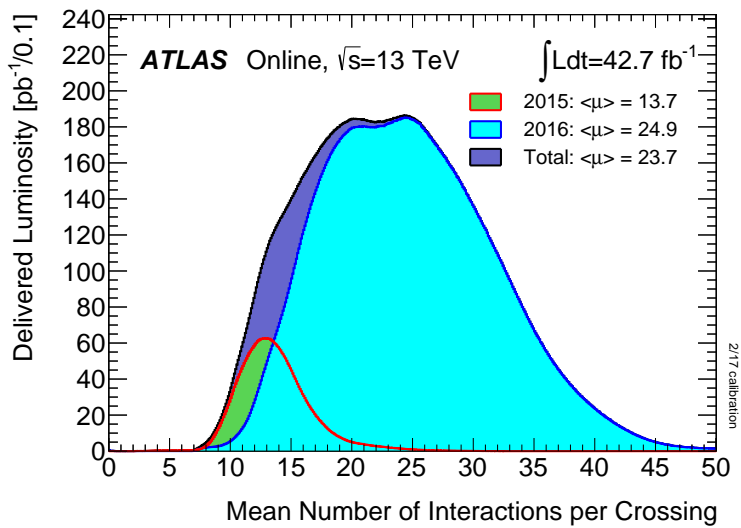


Figure 2.2: The luminosity-weighted distribution of the mean number of interactions per crossing for the 2015 and 2016 pp collision data at $\sqrt{s} = 13$ TeV centre-of-mass energy.⁴

2.2 A TOROIDAL LHC APPARATUS

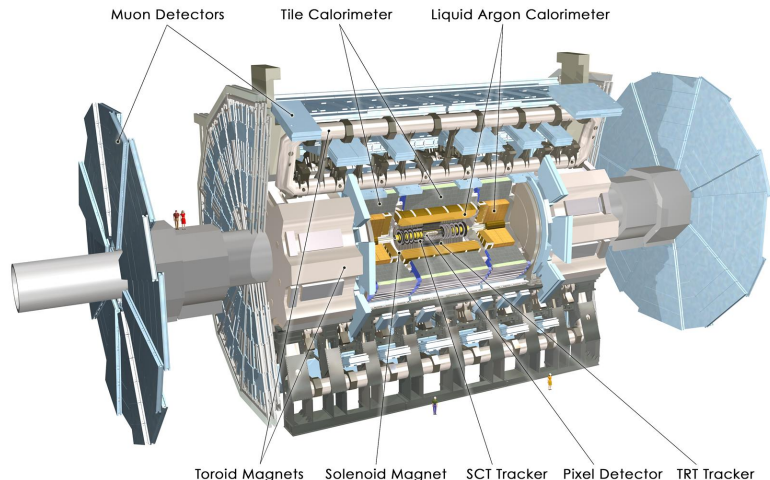


Figure 2.3: A detailed computer-generated image of the ATLAS detector and its systems.

Parameter [unit]	Nominal design value	2015 Operating value	2016 Operating value
Beam Energy [TeV]	7	6.5	6.5
Peak L [$10^{34} \text{ cm}^2 \text{ s}^{-1}$]	1	0.5	1.25
Bunch spacing [ns]	25	25	25
f_{rev} [kHz]	11245	11245	11245
n_b [10^{11} p/bunch]	1.15	1.15	1.12
N_b [bunch]	2808	1825	2220
ϵ_n [mm mrad]	3.5	3.5	2
β^* [cm]	55	20-40	40
F	0.84	0.84	0.59
$\langle \mu \rangle$	19	13	41

Table 2.1: LHC nominal²⁶ and operational parameters in 2015³² and 2016³³.

The ATLAS experiment³⁴ at the LHC is a general-purpose particle detector with a near 4π coverage in solid angle and a forward-backward symmetric cylindrical geometry. The ATLAS detector (Figure 2.3) consists of an inner tracking detector (ID) surrounded by a 2.3 m diameter thin superconducting solenoid providing a 2T axial magnetic field, electromagnetic (EM) and hadronic calorimeters, and a muon spectrometer (MS). Three extra air-core toroid magnets generate the magnetic field in the MS.

2.2.1 COORDINATE SYSTEM

ATLAS uses a right-handed coordinate system with its origin at the nominal IP in the center of the detector and the z -axis along the beam pipe. The x -axis points from the IP to the center of the LHC ring, the y -axis points towards the sky, and the z -axis points straight(like bridges) towards the Geneva airport(A side), back from the Charlie pub in France(C side). Cylindrical coordinates (r, φ) are used in the transverse plane, φ being the azimuthal angle around the z -axis. The pseudorapidity is defined in terms of the polar angle ϑ as $\eta = -\ln \tan(\vartheta/2)$. It is the massless approximation of rapidity, the angle parameterizing special relativity's boosts. Most hadron productions are roughly constant in η , and for two massless particles travelling in different directions, their difference in $\Delta\eta$ is

invariant. Therefore, angular distance is measured in units of $\Delta R = \sqrt{(\Delta\eta)^2 + (\Delta\varphi)^2}$.

The region with $\eta \sim 0$ is called “central”, consisting of the “barrel” elements, surrounding the beam line cylindrically. At high $|\eta| > 2.5$, the region is referred to as “forward”, where “endcap” detector elements are arranged as disks perpendicular to the beam line.

2.2.2 INNER DETECTOR

The ID covers the pseudorapidity range $|\eta| < 2.5$. It consists of three parts: silicon pixel (PIXEL), silicon microstrip (SCT), and straw-tube transition-radiation tracking (TRT) detectors. An additional pixel detector layer (IBL)³⁵, inserted at a mean radius of 3.3 cm, is used in the Run-2 data-taking and improves the identification of b -jets³⁶. A 10 GeV charged particle in the barrel region expects 1 + 3 IBL-Pixel hits, 8 SCT hits and 36 TRT hits.

ID is designed to provide charged particle momentum measurement with $\sigma_{p_T}/p_T \sim 0.05\% p_T \oplus 1\%$ and vertex reconstruction. Because of this, each detector proves measurement accuracies of the order 10 μm in $R\text{-}\varphi$ and 100 μm in z . Figure 2.4a³⁷ shows the $R\text{-}z$ distribution of the material for a quadrant of the barrel region PIXEL and SCT. The intensity of a particle beam decreases exponentially in radiation length. $I(x) = I_0 e^{-x/X_0}$, where I is the intensity, x is the distance traveled, and X_0 is the radiation length. Figure 2.4b shows the distribution of hadronic-interaction vertex candidates in $|\eta| < 2.4$ and $|z| < 400$ mm for 13 TeV data.

2.2.3 CALORIMETER

Lead/liquid-argon (LAr) finely segmented sampling calorimeters provide EM energy measurements. A steel/scintillator-tile hadronic calorimeter (HCal) covers the central pseudorapidity range ($|\eta| < 1.7$). The endcap and forward regions are instrumented with copper/tungsten and LAr calorimeters for both the EM and hadronic energy measurements up to $|\eta| = 4.9$. The calorimeters

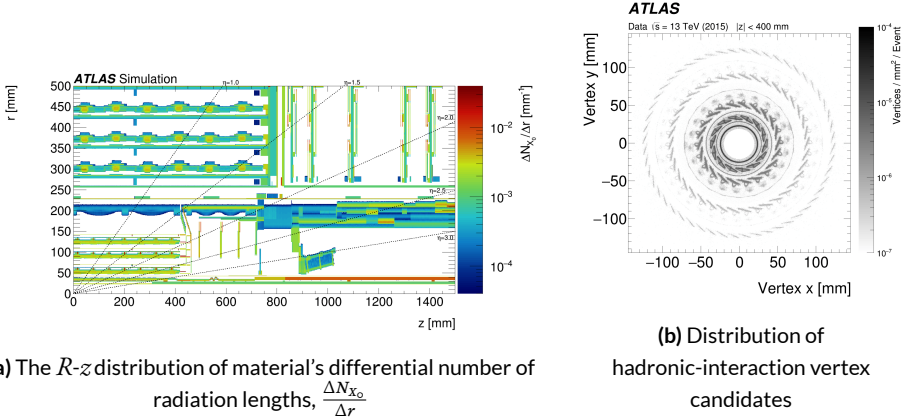


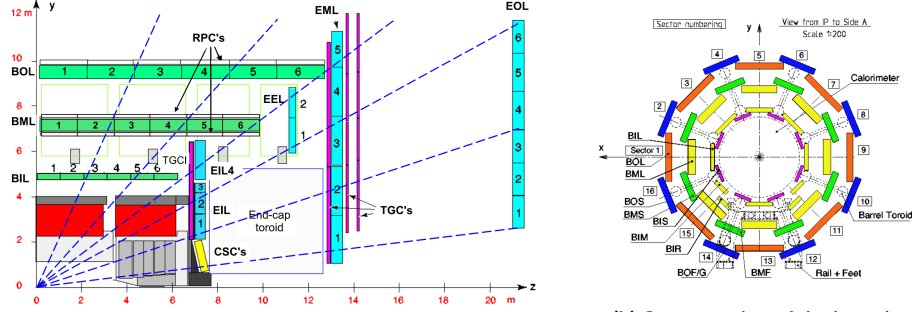
Figure 2.4: Gemoetry of IBL, PIXEL and SCT detectors in Run2.

also provide basic EM/Hadronic trigger information, with fast analogue summing in coarse granularity.

EM calorimeter (ECal) is designed to have > 22 radiation lengths in the barrel and > 24 in the endcap. It provides EM measurement with $\sigma_E/E = 10\%/\sqrt{E} \oplus 0.7\%$. The hadronic calorimeter (HCal) has approximately 9.7 interaction length in the barrel and 10 in the endcap. HCal provides hadronic measurement with $\sigma_E/E = 50\%/\sqrt{E} \oplus 3\%$ in the Barrel and Endcap regions, and $\sigma_E/E = 100\%/\sqrt{E} \oplus 10\%$ in the forward region.

2.2.4 MUON SPECTROMETER

The muon spectrometer (Figure 2.5) surrounds the calorimeters and includes three large superconducting air-core toroids. The field integral of the toroids ranges between 2 and 6 T/m for most of the detector. Because of this bending power, the MS measures Muon momentum stand-alone, with $\sigma_{p_T}/p_T \sim 10\%$ at $p_T = 1\text{TeV}$. Muon Drift Tubes (MDT) and Cathode Strip Chambers (CSC) provide precision tracking. Each MDT has $80\text{ }\mu\text{m}$ spacial resolution, with an alignment precision of $30\text{ }\mu\text{m}$. Resistive Plate Chambers (RPC) in the barrel and Thin Gap Chambers (TGC) provide



(a) Cross-section of the muon system in R - z plane.
Numbers indicate different γ stations. For MDT letters, B means barrel, and E means endcap. I stands for inner, M for middle, O for outer, and E for extra.

(b) Cross-section of the barrel muon system in x - y plane.
Numbers indicate different φ stations. Last L means large sectors and last S means small sectors.

Figure 2.5: The overall layout of the ATLAS MuonSpectrometer.

triggering, with 1.5-5 ns timing resolution. The muon spectrometer defines the overall dimensions of the ATLAS detector.

2.2.5 TRIGGER AND DATA ACQUISITION

A dedicated trigger system is used to select events³⁸. The first-level trigger (L_1) is implemented in hardware and uses the calorimeter and muon detectors to seed regions of interest (RoI) and reduce the accepted event rate to 100 kHz. This is followed by a software-based high-level trigger (HLT) that reduces the accepted event rate to 1 kHz on average. To avoid too high accept rates for certain triggers, the triggers are often prescaled, which means the accepted events get rejected at the prescale. For example, a prescale of two means only every second event passing all trigger conditions gets accepted.

Over 2015 and 2016, both the LHC and the ATLAS performed outstandingly⁴. The total data recording efficiency for ATLAS is around 92%, shown in Figure 2.6.

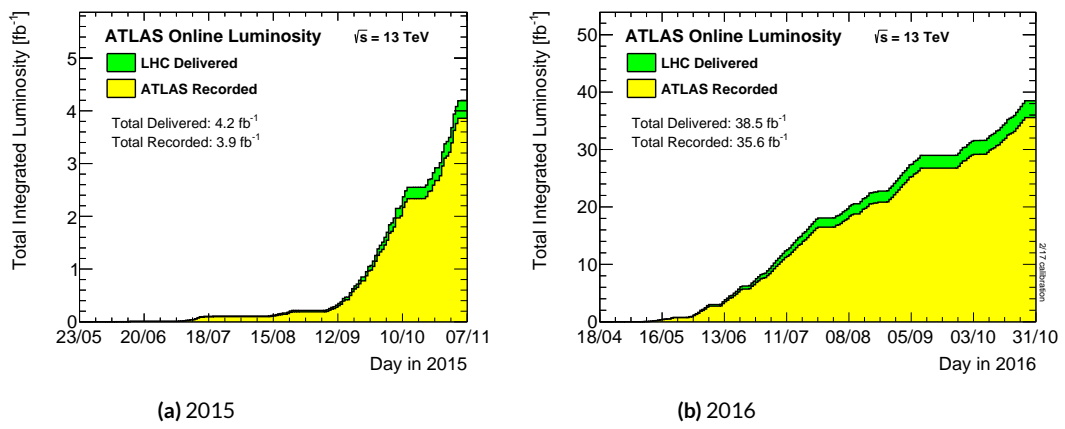


Figure 2.6: Cumulative luminosity versus time delivered to (green) and recorded by ATLAS (yellow) during stable beams for pp collisions at 13 TeV centre-of-mass energy.

“A picture is worth a thousand swords.”

Tony

3

Reconstruction and Objects

Reconstruction is to reform the physics objects from raw detector readouts. In each pp collision recorded by ATLAS, charged particles bend and leave tracks in the ID, electrons and photons deposite their energy in ECAL, hadrons are abosrbed in HCAL, muons leave an extra track in the MS, and neutrinos are inferred by the conservation of momentum in the transverse plane. Figure 3.1 gives an overview of the different sub-detectors that each type of particle will interact with in ATLAS.

Each pp collision generate multiple vertices, and they reconstructed from the available ID tracks. The primary vertex (PV), or the hard-scatter vertex, is selected as the one with the largest $\sum p_T^2$, where the sum is over all tracks with transverse momentum $p_T > 0.4$ GeV that are associated with the vertex. Most physics objects are required to be consistent with the primary vertex.

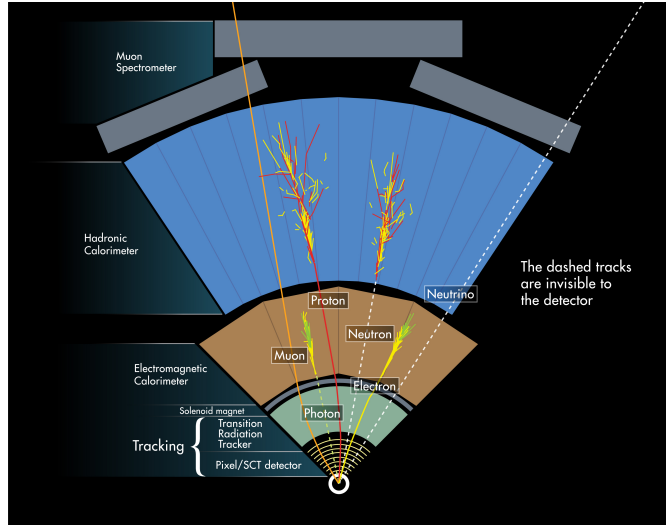


Figure 3.1: Illustration of particle interactions in ATLAS.

3.1 JETS

When a quark or gluon is produced in collisions, it produces a collimated spray of hadrons in the outgoing direction of the parton, which is known as a jet. Jets are built from topological clusters of energy deposits in calorimeter cells³⁹, using a four-momentum reconstruction scheme with massless clusters as input. The directions of jets are corrected to point back to the primary vertex. Jets are reconstructed using the anti- k_t algorithm with different values of the radius parameter R . R appears in the denominator of the clustering distance metric and determines the radial size of the jet in η - φ plane.

3.1.1 SMALL- R JETS

The jets with $R = 0.4$ (“small- R jets”) are reconstructed from clusters calibrated at the electromagnetic (EM) scale. The jets are corrected for additional energy deposited from pile-up interactions using an area-based correction⁴⁰. They are then calibrated using p_T - and η -dependent calibration factors derived from simulation, before global sequential calibration⁴¹ is applied, which reduces dif-

ferences in calorimeter responses to gluon- or quark-initiated jets. The final calibration is based on in situ measurements in collision data⁴².

“small- R jets” are required to be consistent with the primary vertex, in order to avoid contamination from pileup interactions. The jet vertex fraction (JVF) is the ratio of tracks associated with a primary vertex to the total number of tracks inside a jet. Jets from the PV should have most tracks consistent with the PV and therefore have a large JVF value.

3.1.2 LARGE- R JETS

The jets with $R = 1.0$ (“large- R jets”) are built from locally calibrated⁴¹ topological clusters. They are trimmed⁴³ to minimize the impact of energy deposits from pile-up interactions. Trimming proceeds by reclustering the jet with the k_t algorithm⁴⁴ into $R = 0.2$ subjets and then removing those subjets with $p_T^{\text{subjett}}/p_T^{\text{jet}} < 0.05$, where p_T^{subjett} is the transverse momentum of the subjet and p_T^{jet} that of the original jet. The energy and mass scales of the trimmed jets are then calibrated using p_T - and η -dependent calibration factors derived from simulation⁴⁵.

The calorimeter-based jet mass m^{calo} for a large-radius calorimeter jet J is computed from the calorimeter cell cluster constituents i with energy E_i and momentum \vec{p}_i :

$$m^{\text{calo}} = \sqrt{\left(\sum_{i \in J} E_i\right)^2 - \left(\sum_{i \in J} \vec{p}_i\right)^2}. \quad (3.1)$$

For a boosted massive particle, the angular spread in the decay products scales as $\frac{1}{p_T}$. For highly boosted cases, the spread could be comparable with the $\eta \times \varphi \sim 0.1 \times 0.1$ calorimeter granularity. Tracking information can be used to maintain performance beyond this granularity limit. The

track-assisted jet mass, m^{TA} , is defined as:

$$m^{TA} = \frac{p_T^{calo}}{p_T^{track}} \cdot m^{track}. \quad (3.2)$$

where p_T^{calo} is the transverse momentum of the large-R calorimeter jet, p_T^{track} is the transverse momentum of the four-vector sum of tracks associated to the large-R calorimeter jet, and m^{track} is the invariant mass of this four-vector sum. This ratio corrects for charged-to-neutral fluctuations, and there improves the resolution with respect to track-only jet mass.

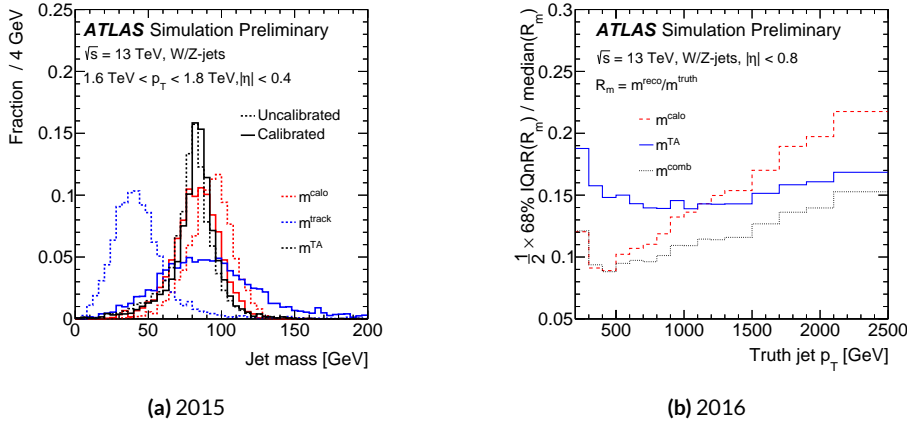


Figure 3.2: Uncalibrated (dashed line) and calibrated (solid line) reconstructed jet mass distribution 3.2a, and the jet mass resolution vs jet p_T 3.2b for calorimeter-based jet mass, m^{calo} (red), track-assisted jet mass m^{TA} (black) and the invariant mass of four-vector sum of tracks associated to the large-radius calorimeter jet m^{track} (blue) for W/Z-jets⁵.

The two mass definitions are only weakly correlated with each other, therefore they can be linearly combined to the combined mass, m^{comb} , by weighting the components with w :

$$m^{comb} = w \cdot m^{calo} + (1 - w) \cdot m^{TA}. \quad (3.3)$$

The weight is determined for each large-R jet from the resolution functions of the calibrated track and calo mass terms. This leads to a smaller mass resolution and better estimate of the median mass

value than obtained using only calorimeter energy clusters, as shown in Figure 3.2.

3.1.3 TRACK JETS

ID track is made first by creating clusters based on PIXEL and SCT measured energy deposits, which are called space-points. Three space-points form a seed, and the seeds are combined to build track candidates using a Kalman filter. After ambiguity solving, an artificial neural network is trained and used to identify merged clusters. The last step is a high resolution fit, which is CPU intensive.

The tracks are required to have $p_T > 0.4 \text{ GeV}$ and $|\eta| < 2.5$, to have at least 1 PIXEL hit and 6 SCT hits, and to be tightly matched to the primary vertex. The performance of track reconstruction is highly dependent on the momentum of the particle. With higher boost, the decay tracks have smaller separations in the inner detector, hindering the resolving cluster process, and thus degrading the track identification efficiency. For a 1 TeV b -hadron, the reconstruction track efficiency is 83%, compared to 95% for a 200 GeV b -hadron ⁴⁶.

Track jets are essentially clustered tracks left by charged hadrons. They are reconstructed from ID tracks using the anti- k_t algorithm with $R = 0.2$. Once the track jet axis is determined, a second step of track association is performed to select tracks with looser impact parameter requirements in order to collect the tracks needed for effectively running the b-tagging algorithms. Only track jets with at least two tracks are considered. They are also required to have $p_T > 10 \text{ GeV}$ and $|\eta| < 2.5$ to suppress trackjets from light flavors.

Track jets are associated to large- R jets using Ghost-Association. “Ghosts” are track jet 4-vectors, with each track jet’s p_T set to an infinitesimal amount, essentially keeping only the direction of the 4-vector. This ensures that Large- R jets reconstruction is not altered by the ghosts when the calorimeter clusters plus ghosts are reclustered. The reclustering is then performed using the anti- k_t algorithm with $R = 1.0$. The calorimeter jets after reclustering are identical to the parents of the trimmed

jets used in this analysis, with the addition of the associated track jets retained as constituents. In addition, if trimming is subsequently performed on this reclustered jet, the track jets corresponding to the ghosts that survive the trimming procedure (and thus are clustered into one of the surviving subjets) are the track jets ghost-associated to the trimmed jet. The small radius parameter of the track-jets enables two nearby b -hadrons to be identified when their ΔR separation is small, which is beneficial when reconstructing high- p_T Higgs boson candidates.

3.2 BOOST

The thesis focuses on searching for TeVsacle resonance decaying into di-Higgs and then to $b\bar{b}b\bar{b}$. It is important to fully reconstruct the decaying object. The angular seperation between the $b\bar{b}$, ΔR_{bb} , scales roughly as $\frac{2m_H}{p_H}$, for a Higgs with momentum p_H decaying into $b\bar{b}$. This means for a 1.5 TeVresonance G_{KK}^* , produced at rest, the two Higgs with each roughly 625 GeVmomentum, and the ΔR_{bb} is around 0.4. Similarly, for a 3 TeVresonace, the 2.75 TeVresonance, ΔR_{bb} is around 0.2.

The ΔR_{bb} limits the object in the analysis. Therefore, two analysis are used to reconstruct the Higgs bosons. The resolved analysis is used for hh systems in which the Higgs bosons have Lorentz boosts low enough that four $R = 0.4$ b -jets can be reconstructed. The boosted analysis is used for those hh systems in which the Higgs bosons have higher Lorentz boosts, which prevents the Higgs boson decay products from being resolved in the detector as separate b -jets. Instead, each Higgs boson candidate consists of a single large-radius jet, and the presence of b -quarks is inferred using smaller-radius jets built from charged-particle tracks. This thesis will be focusing on the boosted analysis.

3.3 FLAVOR TAGGING

Jets are formed from partons with different flavors. Identifying the flavor of a jet is called flavor tagging. Jets originating from a b -quark is referred as a b -jet, from a c -quark is referred as a c -jet, and from other quarks other than the t -quark is referred as a light jet. b -tagging is particularly useful for this analysis, since there are $b\bar{b}b\bar{b}$ in the final state.

B -hadrons have a lifetime on the order of 10^{-12} seconds, which makes a $c\tau$ of $0.5 \text{ mm}^{\textcolor{red}{1}}$. This results in a displaced decay vertex, and it can be identified in vertex reconstruction. This allows b -jets to be distinguished from other flavors of jets theoretically.

ATLAS uses three different basic b -tagging algorithms, that provides complementary information:

- Impact parameter (IP) based algorithm; it uses the transverse and longitudinal impact parameters d_0 and z_0 of the tracks inside a jet to determine their consistency with the primary vertex. It then uses two or three dimensional templates for light flavor, c , and b jets and evaluate the likelihood of the jet coming from each of these types.
- Inclusive secondary vertex (SV) reconstruction algorithm; it uses tracks inside the jet to fit for vertices that are displaced from the primary vertex.
- Decay chain multi-vertex reconstruction algorithm, or JetFitter (JF); it reconstructs the full flight path of the b by looking for multiple displaced vertices along the same direction.

Jets containing b -hadrons are identified using a score value computed from a boosted decision tree(BDT) algorithm $MV2c10$ ^{47,48}, which makes use of observables provided by three algorithms above. The $MV2c10$ algorithm is trained on a sample with charm composition of 7%. It is applied to a set of charged-particle tracks that satisfy quality and impact parameter criteria and are matched to each jet.

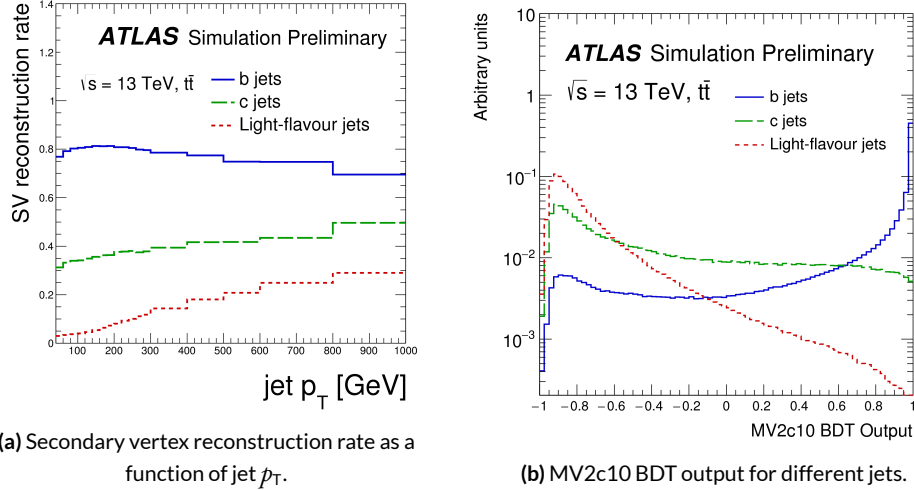


Figure 3.3: Secondary vertex reconstruction rate and Mv2c10 output for b-jets (solid blue), c-jets (dashed green) and light-jets (dotted red) evaluated with simulated $t\bar{t}$ events.

The b -tagging requirements of both the resolved and the boosted analyses use working points that lead to an efficiency of 70% for b -jets with $p_T > 20 \text{ GeV}$ when evaluated in a sample of simulated $t\bar{t}$ events. This working point corresponds to a rejection rate of jets originating from u -, d - or s -quarks or gluons of 380 for the jets with $R = 0.4$ and 120 for the track-jets. The rejection of jets from c -quarks is 12 for the $R = 0.4$ jets and 7.1 for the track-jets.

In the boosted analysis, the track-jets have a wider p_T range, between $50 - 400 \text{ GeV}$, and the same working point leads to b -tagging efficiencies varying from 40% at low p_T , to 80% for p_T values of about 150 GeV, to 60% at high p_T . The increase of tracks from fragmentation in the high jet p_T region is the main reason for the performance degradation. As the jet p_T increases, the number of fake vertices is increasing, while the secondary vertex reconstruction efficiency for b and c jets slightly decreases with jet p_T .

b -jet calibration is done using $t\bar{T}t$ events. Correction factors are applied to the simulated event samples to compensate for differences between data and simulation in the b -tagging efficiency for b , c and light-jets. The correction for b -jets is derived from ttbar events with final states containing two leptons, and the corrections are consistent with unity with uncertainties at the level of a few percent over most of the jet p_T range.

Uncertainties on the correction factors for the b -tagging identification response are applied to the simulated event samples by looking at dedicated flavour-enriched samples in data. An additional term is included to extrapolate the measured uncertainties to the high- pT region of interest. This term is calculated from simulated events by considering variations on the quantities affecting the b -tagging performance such as the impact parameter resolution, percentage of poorly measured tracks, description of the detector material, and track multiplicity per jet. The dominant effect on the uncertainty when extrapolating to high- pT is related to the different tagging efficiency when smearing the track impact parameters based on the resolution measured in data and simulation.

3.4 LEPTONS

Electron and photon identification is based on matching tracks to energy clusters in the ECAL and relying on the longitudinal and transverse shapes of the EM shower⁴⁹. Well-reconstructed ID tracks matched to clusters are classified as electron candidates, while clusters without matching tracks are classified as unconverted photon candidates. Clusters matched to a reconstructed conversion vertex or to pairs of tracks consistent with the conversion hypothesis are classified as converted photon candidates. Eletrons and photons are not used in this thesis.

Hadronic tau decays are composed of a tau neutrino and one or three charged pions and up to two neutral pions⁵⁰. The tau reconstruction is seeded by jets, and matched one or three associated

tracks, with a total electric charge of ± 1 . A Boosted Decision Tree (BDT) identification procedure, based on calorimetric shower shapes and tracking information is used to reject backgrounds from jets. Hadronic taus are not used in this thesis.

Neutrinos are inferred from the missing transverse momentum (MET), or E_T^{miss} . Neutrinos do not interact with the ALTAS. Their presence can only be deduced from the conservation of transverse momentum in each collision, as the incoming protons have no net momentum in the transverse plane. MET is calculated as the negative vectorial sum of the p_T of all fully reconstructed and calibrated physics objects. This procedure includes a “soft term”, which is calculated using the ID tracks that originate from the primary vertex but are not associated with reconstructed objects. MET is not used in this thesis.

Muons are identified by matching ID tracks with reconstructed MS tracks³¹. For this thesis, muons must have $p_T > 4$ GeV, $|\eta| < 2.5$ and to satisfy “medium” muon identification criteria³¹. If a muon is within $\Delta R = 0.4$ (0.2) of a jet used for b -tagging in the resolved (boosted) analysis, their four-momentum is added to the calorimeter-based jet’s four-momentum to partially account for the energy lost in semileptonic b -hadron decays.

Ugliness is in a way superior to beauty because it lasts.

Serge Gainsbourg

4

Data and Simulation

4.0.1 DATA

This analysis is performed on two LHC pp collision datasets at $\sqrt{s} = 13$ TeV recorded by the ATLAS experiment. Data were collected during stable beam conditions and when all relevant detector systems were functional. A Good Run List (GRL) is generated after gathering online and offline data quality reviews of the dataset after reconstruction. Typically, any $> 10\%$ defect in any detector subsystem makes the corresponding Lumibloks (LB) fail the GRL requirement. The integrated luminosity of the 2015 dataset passing the GRL is 3.2 fb^{-1} , and the 2016 dataset passing a different GRL is 32.9 fb^{-1} . These values are about 82% and 92% of the data ATLAS recorded, in Figure 2.6.

In the resolved analysis, a combination of b -jet triggers is used. Events were required to feature either one b -tagged jet^{47,48} with transverse momentum $p_T > 225$ GeV, or two b -tagged jets, either both satisfying $p_T > 35$ GeV or both satisfying $p_T > 55$ GeV, with different requirements on the b -tagging. Some triggers required additional non- b -tagged jets. Due to a change in the online b -tagging algorithm between 2015 and 2016, the two datasets are treated independently until they are combined in the final statistical analysis. After the selection described in Section ??, this combination of triggers is estimated to be 65% efficient for simulated signals with a Higgs boson pair invariant mass, m_{HH} , of 280 GeV, rising to 100% efficiency for resonance masses greater than 600 GeV. During 2016 data-taking, a fraction of the data was affected by an inefficiency in the online vertex reconstruction, which reduced the efficiency of the algorithms used to identify b -jets; those events were not retained for further analysis. This reduces the integrated luminosity of the 2016 dataset for the resolved analysis to 24.3 fb^{-1} .

In the boosted analysis, events were selected from the 2015 dataset using a trigger that required a single anti- k_t jet³ with radius parameter $R = 1.0$ and with $p_T > 360$ GeV. In 2016, a similar trigger was used but with a higher threshold of $p_T > 420$ GeV. The efficiency of these triggers is 100% for simulated signals passing the jet requirements described in Section ??, so the 2015 and 2016 datasets were combined into one dataset.

*It is a far, far better thing that I do, than I have ever
done; it is a far, far better rest that I go to than I have
ever known.*

Charles Dickens

5

Conclusion

Di-Higgs search has a short history, but will have a long future. This thesis presents a search for both resonant and non-resonant production of pairs of Standard Model Higgs bosons has been carried out in the dominant $b\bar{b}b\bar{b}$ channel, using 27.5–36.1 fb^{-1} of LHC pp collision data at $\sqrt{s} = 13 \text{ TeV}$ collected by ATLAS in 2015 and 2016. The search sensitivity of this analysis exceeds that of the previous analysis of the $\sqrt{s} = 13 \text{ TeV}$ 2015 dataset³ for non-resonant signal and also across the entire mass range of 260–3000 GeV for the resonance search, with significantly improvement in the high mass resonance sensitivities. The resolved analysis has each $h \rightarrow b\bar{b}$ reconstructed as two separate b -tagged jets, and the boosted analysis has each $h \rightarrow b\bar{b}$ reconstructed as a single large-radius jet associated with at least one small-radius b -tagged track-jet. The estimated background consists mainly of multi-jet and $t\bar{t}$ events.

No significant excess is observed in the data. Upper limits on the production cross section times branching ratio to the $b\bar{b}b\bar{b}$ final state are set for a narrow-width spin-0 scalar and for wider spin-2 resonances. The bulk RS model with $k/\bar{M}_{\text{Pl}} = 1$ is excluded for masses between 313 and 1362 GeV, and the bulk RS model with $k/\bar{M}_{\text{Pl}} = 2$ is excluded for masses below 1744 GeV. The 95% CL upper limit on the non-resonant production is 147 fb, which corresponds to 13.0 times the SM expectation.

This result confirms the great success of the Standard Model. The Higgs potential shape couldn't be very different from the SM predictions at TeV energy scale. Without any significant excess, the phase space for Beyond the Standard Model physics is further constrained.

Improvement with future Run 2 data could come b -tagging, especially efficiency increase in high p_T region. Other aspects include advanced trigger technologies, which can increase the signal event rate, and improved jet energy and mass resolution, which can increase the purity in selection. Together with the larger dataset, it is possible to double the current resonance search sensitivity. For non-resonance search, combined $|\frac{\lambda}{\lambda_{\text{SM}}}| \sim 10$ is possible at the end of Run 2 in 2020.

For longer perspectives, di-Higgs searches and measurements will continue to be one of the most important analysis. It can constrain or hint the physics Beyond the Standard Model. In 2030 to 2040, the High Luminosity LHC will be able to constrain $|\frac{\lambda}{\lambda_{\text{SM}}}| \sim 1$ with all the different channels from both ATLAS and CMS combined.

For even longer future developments in high energy experiments, all aspects—accelerator, detector, computation and theory—must advance together to answer the questions the Standard Model cannot answer, or find questions the Standard Model didn't ask^{52,53}. Life is short for mankind, and the understanding of the universe is an endless journey. I am deeply honored to be a small part of this odyssey.

References

- [1] C. Patrignani et al. Review of Particle Physics. *Chin. Phys.*, C40(10):100001, 2016. doi: 10.1088/1674-1137/40/10/100001.
- [2] W.J. Stirling. 7/8 and 13/8 TeV LHC luminosity ratios. 2013. URL http://www.hep.physics.ac.uk/~wstirlin/plots/lhclumi7813_2013_v0.pdf.
- [3] Lyndon Evans. The Large Hadron Collider. *Annual Review of Nuclear and Particle Science*, 61(1):435–466, 2011. doi: 10.1146/annurev-nucl-102010-130438.
- [4] ATLAS Collaboration. ATLAS Luminosity Public Results, Run 2. 2015. URL <https://twiki.cern.ch/twiki/bin/view/AtlasPublic/LuminosityPublicResultsRun2>.
- [5] ATLAS Collaboration. Jet mass reconstruction with the ATLAS Detector in early Run 2 data. ATLAS-CONF-2016-035, 2016. URL <https://cds.cern.ch/record/2200211>.
- [6] Kaustubh Agashe, Hooman Davoudiasl, Gilad Perez, and Amarjit Soni. Warped gravitons at the CERN LHC and beyond. *Phys. Rev. D*, 76:036006, 2007. doi: 10.1103/PhysRevD.76.036006.
- [7] Liam Fitzpatrick, Jared Kaplan, Lisa Randall, and Lian-Tao Wang. Searching for the Kaluza-Klein graviton in bulk RS models. *JHEP*, 09:013, 2007. doi: 10.1088/1126-6708/2007/09/013.
- [8] T. D. Lee. A theory of spontaneous t violation. *Phys. Rev. D*, 8:1226–1239, Aug 1973. doi: 10.1103/PhysRevD.8.1226.
- [9] G.C. Branco et al. Theory and phenomenology of two-Higgs-doublet models. *Phys. Rept.*, 516:1, 2012. doi: 10.1016/j.physrep.2012.02.002.
- [10] Graham D. Kribs and Adam Martin. Enhanced di-higgs production through light colored scalars. *Phys. Rev. D*, 86:095023, 2012. doi: 10.1103/PhysRevD.86.095023.
- [11] R. Gröber and M. Mühlleitner. Composite Higgs boson pair production at the LHC. *JHEP*, 06:020, 2011. doi: 10.1007/JHEP06(2011)020.

- [12] Roberto Contino et al. Anomalous couplings in double Higgs production. *JHEP*, 08:154, 2012. doi: [10.1007/JHEP08\(2012\)154](https://doi.org/10.1007/JHEP08(2012)154).
- [13] ATLAS Collaboration. Search for pair production of Higgs bosons in the $b\bar{b}b\bar{b}$ final state using proton–proton collisions at $\sqrt{s} = 13$ TeV with the ATLAS detector. *Phys. Rev. D*, 94:052002, 2016. doi: [10.1103/PhysRevD.94.052002](https://doi.org/10.1103/PhysRevD.94.052002).
- [14] ATLAS Collaboration. Search for Higgs boson pair production in the $b\bar{b}b\bar{b}$ final state from pp collisions at $\sqrt{s} = 8$ TeV with the ATLAS detector. *Eur. Phys. J. C*, 75:412, 2015. doi: [10.1140/epjc/s10052-015-3628-x](https://doi.org/10.1140/epjc/s10052-015-3628-x).
- [15] ATLAS Collaboration. Search for Higgs Boson Pair Production in the $\gamma\gamma b\bar{b}$ Final State Using pp Collision Data at $\sqrt{s} = 8$ TeV from the ATLAS Detector. *Phys. Rev. Lett.*, 114:081802, 2015. doi: [10.1103/PhysRevLett.114.081802](https://doi.org/10.1103/PhysRevLett.114.081802).
- [16] David Griffiths. *Introduction to elementary particles*. 2008.
- [17] Christopher G. Tully. *Elementary particle physics in a nutshell*. 2011.
- [18] Matthew D. Schwartz. *Quantum Field Theory and the Standard Model*. Cambridge University Press, 2014. ISBN 1107034736, 9781107034730.
- [19] ATLAS Collaboration. Observation of a new particle in the search for the Standard Model Higgs boson with the ATLAS detector at the LHC. *Phys. Lett. B*, 716:1, 2012. doi: [10.1016/j.physletb.2012.08.020](https://doi.org/10.1016/j.physletb.2012.08.020).
- [20] CMS Collaboration. Observation of a new boson at a mass of 125 GeV with the CMS experiment at the LHC. *Phys. Lett. B*, 716:30, 2012. doi: [10.1016/j.physletb.2012.08.021](https://doi.org/10.1016/j.physletb.2012.08.021).
- [21] R. Frederix, S. Frixione, V. Hirschi, F. Maltoni, O. Mattelaer, P. Torrielli, E. Vryonidou, and M. Zaro. Higgs pair production at the LHC with NLO and parton-shower effects. *Phys. Lett.*, B732:142–149, 2014. doi: [10.1016/j.physletb.2014.03.026](https://doi.org/10.1016/j.physletb.2014.03.026).
- [22] D. de Florian et al. Handbook of LHC Higgs Cross Sections: 4. Deciphering the Nature of the Higgs Sector. 2016. doi: [10.23731/CYRM-2017-002](https://doi.org/10.23731/CYRM-2017-002).
- [23] Graham D. Kribs, Andreas Maier, Heidi Rzehak, Michael Spannowsky, and Philip Waite. Electroweak oblique parameters as a probe of the trilinear Higgs boson self-interaction. *Phys. Rev.*, D95(9):093004, 2017. doi: [10.1103/PhysRevD.95.093004](https://doi.org/10.1103/PhysRevD.95.093004).

- [24] Viviana Cavalieri and Gabriel Facini. Summary of Limits on BSM Models from Diboson Searches. Technical Report ATL-COM-PHYS-2016-1071, CERN, Geneva, Sep 2016. URL <https://cds.cern.ch/record/2203605>.
- [25] Georges Aad et al. Searches for Higgs boson pair production in the $hh \rightarrow bb\tau\tau, \gamma\gamma WW^*, \gamma\gamma bb, bbbb$ channels with the ATLAS detector. *Phys. Rev.*, D92:092004, 2015. doi: 10.1103/PhysRevD.92.092004.
- [26] Lyndon R Evans and Philip Bryant. LHC Machine. *J. Instrum.*, 3:S08001. 164 p, 2008. URL <https://cds.cern.ch/record/1129806>. This report is an abridged version of the LHC Design Report (CERN-2004-003).
- [27] ATLAS Collaboration. The ATLAS experiment at the CERN Large Hadron Collider. *JINST*, 3:S08003, 2008. doi: 10.1088/1748-0221/3/08/S08003.
- [28] CMS Collaboration. The CMS experiment at the CERN LHC. *Journal of Instrumentation*, 3(08):S08004, 2008. URL <http://stacks.iop.org/1748-0221/3/i=08/a=S08004>.
- [29] LHCb Collaoration. The LHCb Detector at the LHC. *JINST*, 3:S08005, 2008. doi: 10.1088/1748-0221/3/08/S08005.
- [30] ALICE Collaboration. The ALICE experiment at the CERN LHC. *Journal of Instrumentation*, 3(08):S08002, 2008. URL <http://stacks.iop.org/1748-0221/3/i=08/a=S08002>.
- [31] ATLAS Collaboration. Luminosity Determination in pp Collisions at $\sqrt{s} = 7$ TeV Using the ATLAS Detector at the LHC. *Eur. Phys. J.*, C 71:1630, 2011. doi: 10.1140/epjc/s10052-011-1630-5.
- [32] Paul Collier for the LHC team. LHC Machine Status. CERN Resource Review Board, 2015. URL <https://cds.cern.ch/record/2063924/files/CERN-RRB-2015-119.PDF>.
- [33] Giulia Papotti for the LHC team. LHC Machine Status Report. CERN Resource Review Board, 2016. URL https://indico.cern.ch/event/563488/contributions/2277292/attachments/1340292/2019570/20160921_LHCC.pdf.
- [34] ATLAS Collaboration. The ATLAS Experiment at the CERN Large Hadron Collider. *JINST*, 3:S08003, 2008. doi: 10.1088/1748-0221/3/08/S08003.
- [35] ATLAS Collaboration. ATLAS Insertable B-Layer Technical Design Report. CERN-LHCC-2010-013. ATLAS-TDR-19, Sep 2010. URL <https://cds.cern.ch/record/1291633>.

- [36] ATLAS Collaboration. Expected performance of the ATLAS b -tagging algorithms in Run-2. ATL-PHYS-PUB-2015-022, 2015. URL <https://cds.cern.ch/record/2037697>.
- [37] Morad Aaboud et al. Study of the material of the ATLAS inner detector for Run 2 of the LHC. *JINST*, 12(12):P12009, 2017. doi: 10.1088/1748-0221/12/12/P12009.
- [38] ATLAS Collaboration. Performance of the ATLAS Trigger System in 2015. *Eur. Phys. J. C*, 77:317, 2017. doi: 10.1140/epjc/s10052-017-4852-3.
- [39] ATLAS Collaboration. Topological cell clustering in the ATLAS calorimeters and its performance in LHC Run 1. *Eur. Phys. J. C*, 77:490, 2017. doi: 10.1140/epjc/s10052-017-5004-5.
- [40] Matteo Cacciari, Gavin P. Salam, and Gregory Soyez. The catchment area of jets. *JHEP*, 04:005, 2008. doi: 10.1088/JHEP04(2008)005.
- [41] ATLAS Collaboration. Jet energy measurement with the ATLAS detector in proton-proton collisions at $\sqrt{s} = 7$ TeV. *Eur. Phys. J. C*, 73:2304, 2013. doi: 10.1140/epjc/s10052-013-2304-2.
- [42] ATLAS Collaboration. Jet Calibration and Systematic Uncertainties for Jets Reconstructed in the ATLAS Detector at $\sqrt{s} = 13$ TeV. ATL-PHYS-PUB-2015-015, 2015. URL <https://cds.cern.ch/record/2037613>.
- [43] D. Krohn, J. Thaler, and L.-T. Wang. Jet trimming. *JHEP*, 02:084, 2010. doi: 10.1007/JHEP02(2010)084.
- [44] Stephen D. Ellis and Davison E. Soper. Successive combination jet algorithm for hadron collisions. *Phys. Rev. D*, 48:3160, 1993. doi: 10.1103/PhysRevD.48.3160.
- [45] ATLAS Collaboration. Performance of jet substructure techniques for large- R jets in proton–proton collisions at $\sqrt{s} = 7$ TeV using the ATLAS detector. *JHEP*, 09:076, 2013. doi: 10.1007/JHEP09(2013)076.
- [46] M. Aaboud et al. Performance of the ATLAS Track Reconstruction Algorithms in Dense Environments in LHC Run 2. *Eur. Phys. J. C* 77(10):673, 2017. doi: 10.1140/epjc/s10052-017-5225-7.
- [47] ATLAS Collaboration. Optimisation of the ATLAS b -tagging performance for the 2016 LHC Run. *ATL-PHYS-PUB-2016-012*, (ATL-PHYS-PUB-2016-012), Jun 2016. URL <https://cds.cern.ch/record/2160731>.

- [48] ATLAS Collaboration. Performance of b -jet identification in the ATLAS experiment. *JINST*, **11**:Po4008, 2016. doi: [10.1088/1748-0221/11/04/Po4008](https://doi.org/10.1088/1748-0221/11/04/Po4008).
- [49] Electron efficiency measurements with the ATLAS detector using the 2015 LHC proton-proton collision data. Technical Report ATLAS-CONF-2016-024, CERN, Geneva, Jun 2016. URL <http://cds.cern.ch/record/2157687>.
- [50] Measurement of the tau lepton reconstruction and identification performance in the ATLAS experiment using pp collisions at $\sqrt{s} = 13$ TeV. Technical Report ATLAS-CONF-2017-029, CERN, Geneva, May 2017. URL <http://cds.cern.ch/record/2261772>.
- [51] Georges Aad et al. Muon reconstruction performance of the ATLAS detector in proton-proton collision data at $\sqrt{s} = 13$ TeV. *Eur. Phys. J.*, **C76**(5):292, 2016. doi: [10.1140/epjc/s10052-016-4120-y](https://doi.org/10.1140/epjc/s10052-016-4120-y).
- [52] Burton Richter. High Energy Colliding Beams; What Is Their Future? *Rev. Accel. Sci. Tech.*, **7**:1–8, 2014. doi: [10.1142/9789814651493_0001](https://doi.org/10.1142/9789814651493_0001),[10.1142/S1793626814300011](https://doi.org/10.1142/S1793626814300011).
- [53] Stephen Hawking and Gordon Kane. Should China build the Great Collider? 2018.